ACS APPLIED MATERIALS & INTERFACES

Research Article

Cite This: ACS Appl. Mater. Interfaces 2019, 11, 33043−33053

www.acsami.org

In Situ Observation of the Insulator-To-Metal Transition and Nonequilibrium Phase Transition for $Li_{1-x}CoO_2$ Films with Preferred (003) Orientation Nanorods

Yue Chen,[†,‡,⊥] Qing Yu,[†,‡,⊥] Guigui Xu,[†,‡] Guiying Zhao,[†,§] Jiaxin Li,[*,†,§] Zhensheng Hong,[†,‡] Yingbin Lin,[†,‡] Chung-Li Dong,[*,∥] and Zhigao Huang[*,†,§]

[†]College of Physics and Energy, Fujian Normal University, Fujian Provincial Key Laboratory of Quantum Manipulation and New Energy Materials, Fuzhou 350117, China

[‡]Fujian Provincial Engineering Technical Research Centre of Solar-Energy Conversion and Stored Energy, Fuzhou 350117, China

[§]Fujian Provincial Collaborative Innovation Center for Optoelectronic Semiconductors and Efficient Devices, Xiamen 361005, China

[∥]Department of Physics, Tamkang University, 151 Yingzhuan Road, Tamsui 25137, Taiwan

Supporting Information

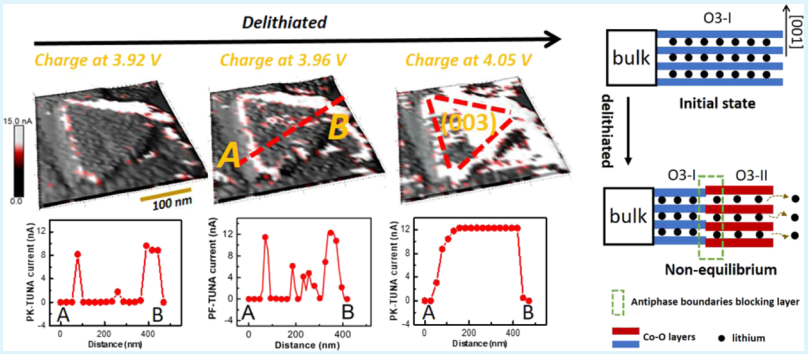

ABSTRACT: It is notoriously difficult to distinguish the stoichiometric $LiCoO_2$ (LCO) with a O3-I structure from its lithium defective O3-II phase because of their similar crystal symmetry. Interestingly, moreover, the O3-II phase shows metallic conductivity, whereas the O3-I phase is an electronic insulator. How to effectively reveal the intrinsic mechanism of the conductivity difference and nonequilibrium phase transition induced by the lithium deintercalation is of vital importance for its practical application and development. Based on the developed technology of in situ peak force tunneling atomic force microscopy (PF-TUNA) in liquids, the phase transition from O3-I to O3-II and consequent insulator-to-metal transition of LCO thin-film electrodes with preferred (003) orientation nanorods designed and prepared via magnetron sputtering were observed under an organic electrolyte for the first time in this work. Then, studying the post-mortem LCO thin-film electrode by using ex situ time-dependent XRD and conductive atomic force microscopy, we find the phase relaxation of LCO electrodes after the nonequilibrium deintercalation, further proving the differences of the electronic conductivity and work function between the O3-I and O3-II phases. Moreover, X-ray absorption spectroscopy results indicate that the oxidation of Co ions and the increasing of O 2p−Co 3d hybridization in the O3-II phase lead to electrical conductivity improvement in $Li_{1-x}CoO_2$. Simultaneously, it is found that the nonequilibrium deintercalation at a high charging rate can result in phase-transition hysteresis and the O3-I/O3-II coexistence at the charging end, which is explained well by an ionic blockade model with an antiphase boundary. At last, this work strongly suggests that PF-TUNA can be used to reveal the unconventional phenomena on the solid/liquid interfaces.

KEYWORDS: *lithium batteries, $LiCoO_2$ thin-film electrode, in situ peak force tunneling AFM, nonequilibrium phase transition, X-ray absorption spectroscopy*

1. INTRODUCTION

Layered transition-metal oxide (LTMO) remains the most researched and commonly used cathode material in lithium/sodium-ion battery by scientists.[1−3] As all the stoichiometric lithium/sodium-based LTMOs can be derived from the prototype structure of $LiCoO_2$,[4] studies on its crystal structure and intrinsic physical properties during deintercalation are indispensable for optimizing the LTMO cathode materials.

Received: June 25, 2019
Accepted: August 16, 2019
Published: August 16, 2019

DOI: 10.1021/acsami.9b11140
ACS Appl. Mater. Interfaces 2019, 11, 33043−33053

$LiCoO_2$, which has a structure similar to $NaCoO_2$ with alkali metal alternate stacking of layers and two-dimensional CoO_2 layers, was first reported as a cathode material for batteries in 1980.[5] After the discovery of excellent thermoelectric properties of Na_xCoO_2,[6] there has been intense interest in the insulator-to-metal transition (IMT) of layered $Li_{1-x}CoO_2$.[7−11] By using the electrochemical delithiated method, Motohashi et al. obtained a series of bulk samples of $Li_{1-x}CoO_2$ with different Li contents.[8] The measured results of the resistivity indicated that the $Li_{1-x}CoO_2$ samples exhibit a semiconductivity for $x < 0.06$, while doing metallic conductivity for $0.25 < x < 0.50$. Miyoshi et al. have also successfully prepared $Li_{1-x}CoO_2$ with different Li contents by chemically extracting lithium from $LiCoO_2$ single crystals.[9] They found that the $LiCoO_2$ single crystals change from an insulator to metal at the critical Li content near $x = 0.10$. However, to date, all the above measurements on conductivity of $Li_{1-x}CoO_2$ have been so far limited to the polycrystal films or microsized single crystals through the four-probe method, so that the influences of the grain boundary resistance and the contact resistance become significant. A recent study investigated the electrical conductivity of delithiation of LCO grains using conductive atomic force microscopy (C-AFM) and high-resolution scanning electron microscopy,[10] which has greatly contributed to our understanding of the IMT at the nanoscale. However, it still should also be noted that the electronic state of static-state LCO samples will be influenced by the Co^{3+}/Co^{4+} charge ordering or Li-ions/vacancy ordering that may not exist in the LCO cathode during the charging/discharging.[11] Therefore, in situ characterizations on the dynamic evolution of intrinsic conductivity of LCO at the nanoscale are highly desirable.

Despite the controversies on the type of IMT in LCO, the Mott[12] or Anderson[13] type transition, the unconventional electric properties of $Li_{1-x}CoO_2$ with different Li contents should be ascribed to its intriguing crystal structure transformations during de-/intercalation.[14−19] The crystal structure evolutions of LCO upon deintercalation have been studied by in situ XRD/neutron diffraction (ND),[20] in situ nuclear magnetic resonance (NMR),[9,21] in situ surface plasmon resonance microscopy (SPRM),[22] ex situ spherical aberration-corrected scanning transmission electron microscopy (STEM),[17] and theoretical calculations.[14,23] It is now well accepted that thermodynamically stable LCO phase with an O3-type structure (called O3-I) undergoes complex phase transitions upon equilibrium deintercalation: (1) the first structure transition of $Li_{1-x}CoO_2$ occurs at a region near $x \approx 0.07-0.25$, where the newly appeared O3-II phase coexists with the pristine LCO O3-I phase (note that the two coexisting phases have the same crystal symmetry except for a 0.7% difference in the lattice constant c). In situ NMR results have provided direct evidence that a Knight-shifted signal emerged at this region, corresponding to the formation of an electrically conductive O3-II phase LCO;[21] (2) the O3-II phase dominates the solid-solution region spanning from $x \approx 0.25$ to 0.5; (3) when half of the lithium was extracted ($x \approx 0.5$, at a near voltage of 4.2 V Li/Li^+), the O3-II phase transforms to a monoclinic phase, and the ordered arrangements of in-plane Li ion and Li vacancy were observed.[17,24] The cutoff charge voltage of the commercial LCO cathode was restricted to 4.2 V Li/Li^+ because further extracting Li-ions out will cause an irreversible phase transition between H1−3, O3 and O1 phases.[14,25]

In situ characterization techniques enable the observation of the dynamic process of phase transition. Among the aforementioned in situ characterization techniques, in situ STEM shows the highest spatial resolution in the dynamic characterization of the crystal structure.[26,27] Gong et al. have observed the coherent twin boundaries and antiphase domain boundaries rising upon charge in the LCO cathode by in situ STEM.[27] However, unfortunately, in the early stage of O3-I → O3-II phase transition, STEM seems to be incapable of distinguishing the two LCO phases because of only a tiny change of the CoO_2 interlayer distance for both phases. Hence, for studying the phase transition between O3-I and O3-II in the LCO cathode, the key challenge remains to develop an in situ experimental technique not only with high temporal and spatial resolution, but also with high sensitivity to the Li-ion movement or Li-ion contents within the electrode lattice structure. In situ SPM has shown its versatility in the field of operando characterizations on battery materials.[28−30] Being different from the early in situ atomic force microscopy (AFM)[31] that only provides morphology information, the recently reported in situ SPM has been tailored to probe specific physical and chemical information in liquid organic electrolytes, such as rate constant of heterogeneous reaction,[32,33] surface electrochemical potential,[34] Young's modulus, conductivity,[35] and so on. The key information of concern here is the conductivity on solid/liquid interfaces that can be captured by peak force tunneling AFM (PF-TUNA) in liquids.[36] By using this new technology, the phase transition from the insulated O3-I phase to the metallic O3-II phase of LCO nanograins may be in situ measured in a liquid electrolyte environment.[37]

Another significant advantage of in situ characterization is to study the nonequilibrium structural dynamics in electrode materials during de-/intercalation under operando conditions. To meet the needs of high power output and rapid charging, the phase transition of electrode materials often takes place under nonequilibrium conditions in practical batteries.[38,39] In situ XRD/ND/TXM analyses have been introduced to observed the state of charge heterogeneity within the cathode electrodes or aberrant phase transition inside the cathode particles under a nonequilibrium delithiated condition, including $LiNi_xMn_{2-x}O_4$,[40,42] $LiFePO_4$,[41,43,45] and $LiCoO_2$.[44] Singer et al. studied nonequilibrium structural dynamics in the $LiNi_{1/2}Mn_{3/2}O_4$ cathode material upon fast de-/intercalation using operando coherent X-rays.[40] Interestingly, they found that, in the phase-transition region with a low lithium concentration, the $LiNi_{1/2}Mn_{3/2}O_4$ cathode undergoes a pure solid solution reaction during lithium extraction, whereas a concurrent solid solution and two-phase reactions were found during lithium intercalation. Zhang et al. further observed an inhomogeneous solid-solution transformation process within a single nanoparticle accompanied with an unexpected reversal of Li concentration,[43] which provides a concrete evidence of solid-solution transformation of $LiFePO_4$ during fast lithiation predicted by Malik et al.[46] To sum up, the characterization of the nonequilibrium de-/intercalation process may help us to discover exotic material properties exhibited not in the equilibrium state. The exotic phase-transition phenomenon, under the nonequilibrium condition, of $LiFePO_4$, $LiNi_{1/2}Mn_{3/2}O_4$, and $LiNi_{1/3}Mn_{1/3}Co_{1/3}O_2$,[47] have been studied. However, the phase-transition images of LCO under far-from-equilibrium processes are not understood well.

DOI: 10.1021/acsami.9b11140
ACS Appl. Mater. Interfaces 2019, 11, 33043−33053

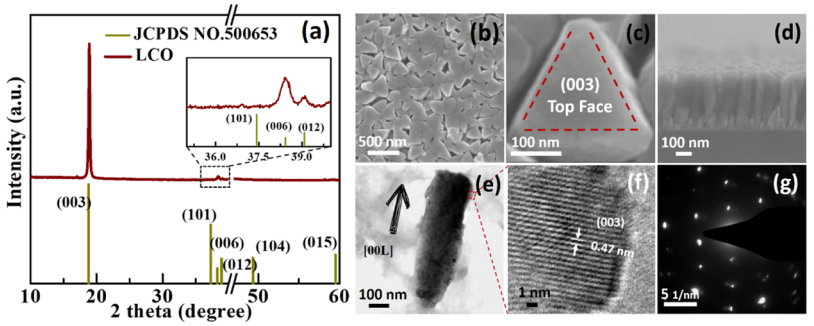

Figure 1. (a) XRD pattern and (b) SEM images for an as-deposited LCO film surface. (c) Typical LCO grain shape. (d) SEM image of a cross section of an LCO thin film and (e) TEM image of an LCO nanorod. (f) HRTEM image and (g) SAED at the top region of the LCO nanorod.

In this work, polycrystalline $Li_{1-x}CoO_2$ thin-film electrodes with the (003) preferable orientation nanograins were deposited by magnetron sputtering. During the first charge, we observed the heterogeneous phase transition from O3-I to O3-II and IMT on the nanograins under the nonequilibrium deintercalation by in situ SPM. The origin of IMT was discussed through combining X-ray absorption spectroscopy (XAS) and first-principles calculation. Besides, by performing the ex situ C-AFM, the intrinsic physical properties of local regions on deintercalated LCO nanograins with different Li contents were also discussed in detail. By performing in situ XRD, we studied the O3-I → O3-II phase transition of LCO thin-film electrodes under different charging rates. The remnant of O3-I were found under high-rate charging, which indicates a remarkable hysteresis of the O3-I phase in the nonequilibrium phase transformations. Moreover, combining with a post-mortem XRD analysis of the deintercalated LCO, it is confirmed that the different conductivities in the local region are corresponding to metastable O3-I, O3-II, and O3-I/II coexisting phases, which will partially be relaxed under an argon protection atmosphere. At last, the ionic blockade mechanism was proposed to understand this fast-extracting process.

2. EXPERIMENTAL SECTION

2.1. Film Electrode Preparation. Polycrystalline $Li_{1-x}CoO_2$ films with the (003) preferable orientation were grown on an aluminum current collector (Macklin, purity 99.0%) using radio-frequency magnetron sputtering. The size of the substrates for sputtering is a square with 2.5 cm on a side. The deposition chamber was evacuated with a turbomolecular pump down to an initial pressure of 4×10^{-4} Pa. During the deposition, the Li-rich target (Li/Co/O = 1.2:1:2) was located on the bottom of the chamber and the power density was kept at 6.11 W/cm^2. Deposition was conducted in a total gas flow amount of 50 sccm and the gas flow ratio of Ar/O_2 was kept at 4:1. The LCO films were deposited for 4 h at a working pressure of 0.5 Pa. In order to improve the film crystallinity, the substrate temperature was maintained at 500 °C. The distance between the target and the rotated substrate was fixed at 10 cm.

2.2. Characterization. The crystalline structure and orientation of the as-deposited LCO films were determined by X-ray diffraction (Rigaku Ultima IV, Cu Kα_1 radiation, λ = 0.15406 nm), and Raman spectroscopy (HORIBA JobinYvon Evolution, laser excitation at 532 nm). The surface morphologies were analyzed by scanning electron microscopy (SEM, Hitachi SU-8010). The in situ PF-TUNA and ex situ C-AFM were performed based on the Bruker Dimension Icon integrated test system. The Li/Co rate of the as-deposited LCO film was determined to be 0.996, as estimated by using an inductively coupled plasma spectrometer (ICP, PerkinElmer Optima 8000). The LCO thin films used for time-dependent XRD measurement were deintercalated under a constant charge rate of 1 C till half of the lithium in the thin-film electrode was extracted. Then, the cells were disassembled, washed in the glovebox, and transferred by a vacuum package for the ex situ time-dependent XRD characterization. The LCO samples for ex situ C-AFM and XAS characterization were obtained by the galvanostatic method and disassembling the half-cell under the argon protective atmosphere. The XAS measurements were performed on the LCO thin-film electrode at different charge states at room temperature.

The in situ PF-TUNA and in situ XRD half-cell were assembled in an Ar-filled glove box with LCO film as the cathode, Li foil as the anode, and 1 M $LiPF_6$ in the mixture solution of ethylcarbonate, ethyl methyl carbonate, and dimethyl carbonate (1:1:1 vol %) as the liquid electrolyte. For the PF-TUNA test, galvanostatic charge of the LCO films was carried out at a moderate current of 16 μA between 3 and 4.2 V. The effective area of the cathode thin films for in situ PF-TUNA characterization is about 0.64 cm^2, and the thickness of cathode thin films is about 400 nm. The in situ XRD spectra were collected from samples at a set interval as the samples were charged by the galvanostatic method. In order to ensure the consistency of the LCO thin film with the in situ PF-TUNA test, the cells were charged at the same current density.

2.3. DFT Calculation. First-principles calculations were performed using the Perdew–Burke–Ernzerhof exchange correlation parameterization to density functional theory (DFT) with the spin-polarized generalized gradient approximation (GGA). The projected augmented wave method was used, as implemented in the Vienna ab initio simulation package (VASP). The on-site electron–electron interactions were taken into account by performing GGA + U level calculations for Co 3d electrons, with U = 4.91 eV taken from the literature.[48] In the energy and electronic properties' calculations, the Gaussian smearing method was used, and the width of smearing was chosen as 0.2 eV. Li_xCoO_2 calculations were performed with a 2 × 2 × 1 supercell. The plane-wave basis set for the kinetic energy cutoff was 550 eV. The Brillouin zone was sampled using the Monkhorst–Pack scheme with a 4 × 4 × 2 k-point grid. Lattice constants and internal co-ordinates were considered to be fully optimized when residual Hellmann–Feynman forces were smaller than 0.01 eV Å^{-1}.

3. RESULTS AND DISCUSSION

Figure 1a shows the XRD pattern of the as-deposited LCO film. The XRD pattern contains a strong diffraction peak at $2\theta \approx 18.9°$ attributed to rhombohedral LCO(003) planes, and two weak diffraction peaks at around 38.4° and 39.0°, attributed to the second-order diffraction peak (006) and LCO(012) planes, respectively. The Raman spectra in Figure S1 also confirm that the as-prepared thin films have vibration modes of an $R\bar{3}m$ HT-LCO structure. From the XRD pattern, one can find that the as-deposited LCO thin films show good crystallization with the (003) preferred orientation, that is, the Li layers are parallel to the substrate. Figure 1b shows SEM images of the LCO thin-film surface. A typical LCO grain shape's top-view is given in Figure 1c. The SEM image shows

DOI: 10.1021/acsami.9b11140
ACS Appl. Mater. Interfaces 2019, 11, 33043–33053

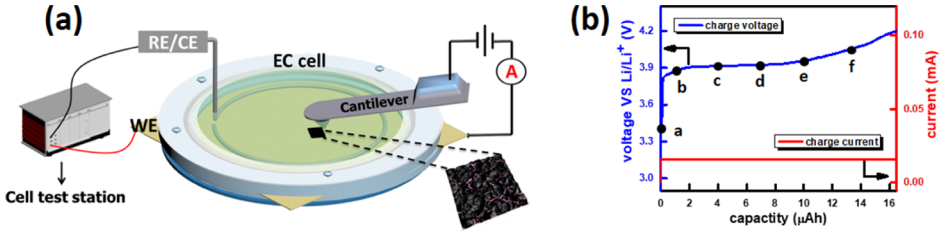

Figure 2. (a) Sketch of the in situ PF-TUNA test technique. (b) Charge curve of the LCO thin film in the EC-cell.

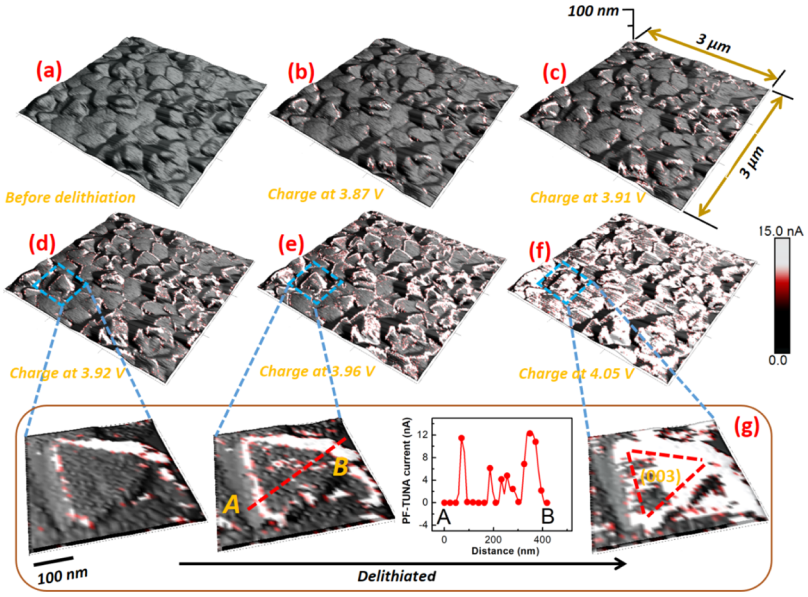

Figure 3. (a–f) Spatial distribution of the TUNA current on the film surface before and during deintercalation, and the corresponding charge points are annotated on the charge curve, Figure 2b. (g) TUNA current on the surface of a typical LCO grain and TUNA current sectional diagram.

that the film contains many close-packed LCO grains with "triangular piece" top structure, and the top face is attributed to the LCO(003) planes. The cross-sectional SEM image in Figure 1d further confirms that the as-prepared LCO thin films consist of many nanorods with the "triangular piece" on top. In order to determine the crystal orientation of the LCO nanorods, the LCO thin film was scraped off and dispersed ultrasonically for transmission electron microscopy (TEM) characterization. Moreover, the lattice constants and the crystal symmetry of both the target and the films have been discussed and compared with that of the substrate, as shown in Table S1 and Figure S2. The high-resolution TEM (HRTEM) image in Figure 1f was captured at the top region of a lying down LCO nanorod in Figure 1e. The details of the scraped samples are in Figure S3. The HRTEM image shows a clear interplanar spacing of ~0.47 nm corresponding to the interplanar distance of the Co–O layers. High crystallinity was also confirmed by selected area electron diffraction (SAED) in Figure 1g. The HRTEM image unambiguously supports that the top face is attributed to the LCO(003) planes. The (003) preferred LCO thin-film electrodes with sluggish Li-ion dynamics can be used as an ideal model for the study of the nonequilibrium delithiated process.

In situ PF-TUNA in liquids allows one to perform nanoscale conductance measurements in an organic electrolyte.[36] By using this technique, measuring simultaneously the morphology and nanoelectrical imaging in liquids becomes possible. Hence, we introduced in situ PF-TUNA to observe the conductivity distribution on the LCO electrode/electrolyte interface in the charge/discharge processes, as shown in the sketch of Figure 2a. The LCO film was used as the work electrode (WE), whereas lithium was used as both the reference electrode and the counter electrode. The electrodes and nanotip were placed in the electrochemical cell (EC cell), then immersed in an organic electrolyte. The cell was charged by the galvanostatic method at a current of 16 μA (corresponding to about 1 C charge rate). The electrochemical performances of LCO thin-film electrodes are given in Figure S4. With the WE potential rising from the initial open circuit voltage to 4.2 V, a −100 mV dc was applied between the nanotip (Pt-coated tip apex with ~50 nm end-tip diameter) and WE for conductivity characterization. During scanning, a constant peak force of 20 nN was applied between the probe and the sample surface, and the system continues to collect the responsive no-faradic current. The tip current captured during the scan was derived from direct contact conduction between the metal tip apex and the grain surfaces, which represents semiquantitatively the local conductivity of the mapping region. The larger the current is, the better the local conductivity is. Here, the current captured by the tip is the no-faradaic current and designated as "TUNA current". Figure 2b shows the charge curve of the LCO thin-film in situ cell. From the figure, a potential plateau at about 3.93 V is found, which indicates the phase transition from the O3-I to the O3-II phase.[49−52] This confirms that the EC cell can work well as a half-cell for studying the electrochemical performance of WE.

Figure 3a–f shows the spatial distributions of TUNA current before and during the delithiation on a 3 × 3 μm^2 scanning

DOI: 10.1021/acsami.9b11140
ACS Appl. Mater. Interfaces 2019, 11, 33043−33053

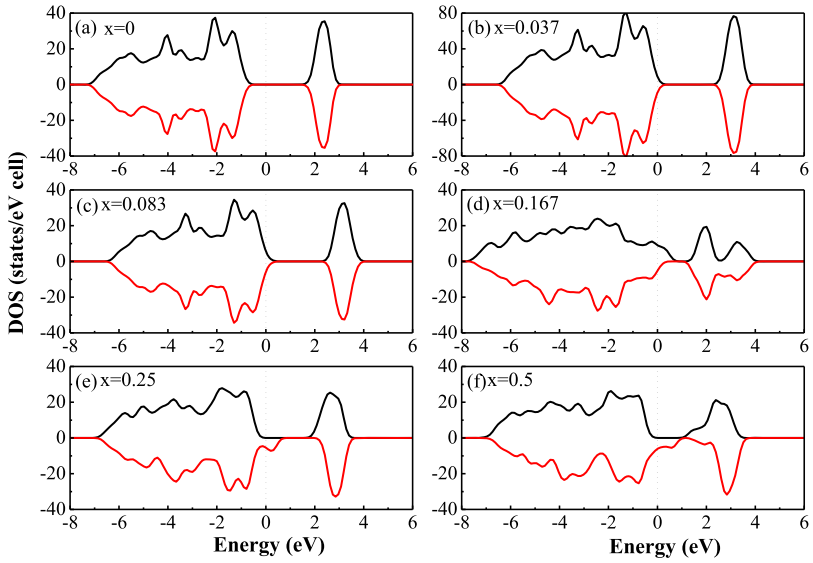

Figure 4. Spin-polarized total DOSs of $Li_{1-x}CoO_2$ with x = 0, 0.037, 0.083, 0.167, 0.25, and 0.5. The Fermi level is set as zero.

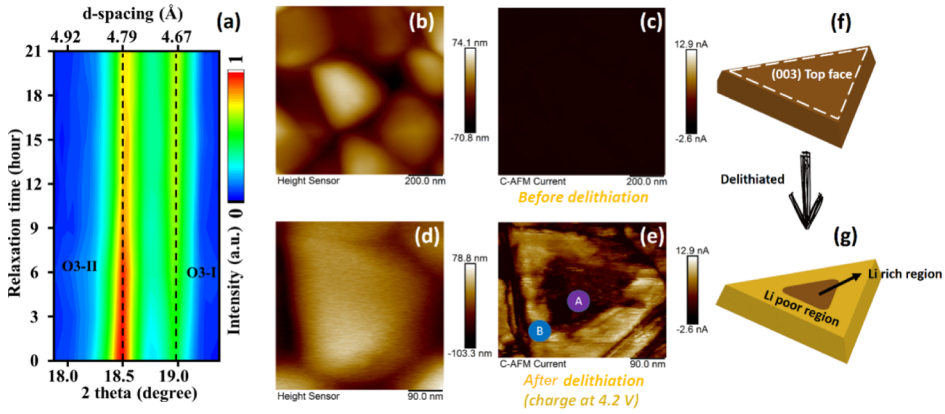

Figure 5. (a) Time-dependent XRD for the post-mortem LCO thin-film electrode obtained by 1 C charging to 4.2 V. (b,c) Grain morphology and current map of $Li_{1-x}CoO_2$ films before delithiating by C-AFM. (d,e) Grain morphology and current map of $Li_{1-x}CoO_2$ films after delithiating by C-AFM. (f,g) Sketch of Li-ion deintercalation from an LCO grain by shrinking core deintercalation models.

area with charge voltage V_c = 3.87, 3.91, 3.92, 3.96, and 4.05V, which are corresponding to a, b, c, d, e, and f charged sites in Figure 2b. As seen in Figure 3a, the average TUNA current of the film before deintercalation is close to the leakage current (~180 pA), which indicates that the film possesses a low conductance in its pristine state, corresponding to the insulated O3-I phase. However, with deintercalation of Li-ions, the TUNA current on the local region around the edge of a triangular piece was abruptly increased, as shown in Figure 3b–e. The increase of current signal at those specific local regions directly results from its conductivity enhancing, which is consistent with the measured results of the resistivity.[8] The abrupt change of current signal means the opportune formation of the metallic O3-II phase. Moreover, the observed uneven spatial distribution of the TUNA current should also reflect the heterogeneity of the phase transition from the O3-I to the O3-II phase on the electrode surface. The smaller scan area (400 × 400 nm^2) including a typical LCO nanograin is also shown in Figure 3g. From the spatial distribution of TUNA current on a typical LCO grain, one can clearly find that the current signal in the edge region occurs earlier than in the inside region, and increased by roughly 2 orders of magnitude compared to the initial leakage current. This indicates that the conductivity drop does first occur in the edge of the delithiated region. Clearly, the surface conductivity change of the LCO thin-film electrode upon charge has been directly observed, and the film surface is found to consiste of two different kinds of regions with a huge conductivity difference in the charging process. The conductivity distribution on the polycrystalline LCO thin-film electrodes, observed by in situ conductivity measurements, strongly confirms that the IMT is prone to occur on the planar edge of the (003) faces. Consequently, the anisotropic IMT may cause uneven conductivity distribution in the electrodes inside the LIBs, which will induce an abnormal concentration of stresses,[29] unequally distributed intercalation/deintercalation process,[44] and discontinuously covered cathode electrolyte interphase.[53] These phenomena can degrade the performance of the LCO electrode.

To understand the observed increasing electron conductivity upon delithiation, the density of states (DOSs) of $Li_{1-x}CoO_2$ with x = 0, 0.037, 0.083, 0.167, 0.25, and 0.5 were calculated from first-principles calculations, as shown in Figure 4. From the figure, it can be seen that the DOS for x = 0 ($LiCoO_2$) evidences insulating behavior with a band gap of 2.05 eV, which is consistent with the experimental data with about 1.7–

DOI: 10.1021/acsami.9b11140
ACS Appl. Mater. Interfaces 2019, 11, 33043–33053

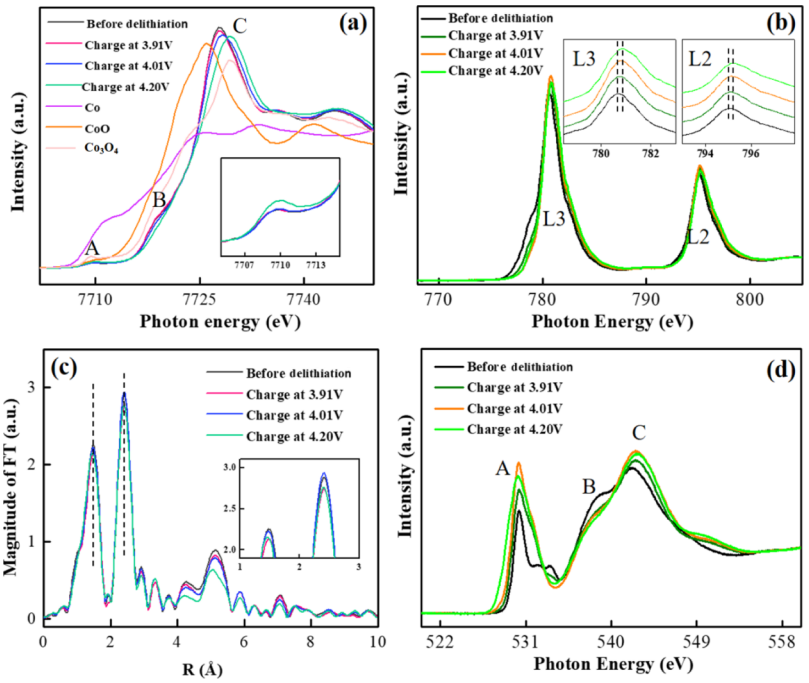

Figure 6. (a,b) Co K-edge and L3,2-edge XAS spectra of $Li_{1-x}CoO_2$ at different charge states and the standard samples. (c) k^3-weighed Fourier transform spectra in the Co K-edge for $Li_{1-x}CoO_2$ at different charge states. (d) O K-edge XAS spectra of $Li_{1-x}CoO_2$ at different charge states.

2.7 eV.[54−57] By contrast, the DOSs for x = 0.037, 0.083, 0.167, 0.25, and 0.5 exhibit nonzero electron density at the Fermi level, thereby reflecting metallic behavior. Thus, the conductivity of $Li_{1-x}CoO_2$ will increase with lithium deintercalation because of the IMT. Ideally, the local region with the high conductivity in the current images can be considered to correspond to the Li-poor location, and the low conductivity region does to the Li-rich state. The calculated results are consistent with the experimental results in Figure 3.

In order to understand better the intrinsic property in an "off-line" condition and also confirm the phase composition, time-dependent XRD and C-AFM were introduced as both are powerful tools to study the intrinsic properties in different areas of the grain after deintercalation. At first, the phase composition and stability in the LCO electrode after deintercalation were studied. Figure 5a shows the time-dependent XRD patterns of the post-mortem LCO thin-film electrode measured under argon protection atmosphere. Here, the peaks at about 18.5° and 19.0° are corresponding to the (003) peaks of the O3-II and O3-I phases. From the figure, it is found that both (003) diffraction peak bands were observed on the spectra. Moreover, one can observe that the relaxation of phase composition is accompanied by the diffraction intensity decrease of the O3-II phase and increase of the O3-I phase, or maybe the increase of the intermediate phase.[47] However, the intensity and site of the diffraction peaks stay almost constant after 10 h, which indicates that the relaxation happens most in the several hours after the electrode disassembled. This relaxation process is consistent with the other layer-structured cathode, $LiNi_{1/3}Mn_{1/3}Co_{1/3}O_2$, in previous reports.[47] The relaxation of phase composition should result from a potential difference between the more delithiated area and the less delithiated area under nonequilibrium deintercalation.[58] Interestingly, as shown in Figure 5a, the relaxation is also accompanied by the increase of the diffraction angle 2θ, which indicates the decrease of interplanar spacing of O3-II. Combining with the above in situ conductivity characterization, the post-mortem XRD analysis confirmed that the high conductivity region (Li-poor region) corresponds to the O3-II phase, and the lower conductivity region is the pristine O3− I phase.

Figure 5b,c shows the surface morphology of the LCO electrode before deintercalation and corresponding C-AFM current map. Here, the C-AFM current was stimulated by the tip with a constant force of 50 nN and dc of −1 V. The tip bias was set below the threshold of Li-ion migration voltage to generate the no-faradic current. In other words, the C-AFM current captured by the tip is mostly attributed to the movement of electrons instead of the Li-ions.[59] As shown in the C-AFM current map, the film surface is almost insulative (O3-I phase) before deintercalation wherever the (003) face or the other region. However, from the C-AFM map of a typical grain of the delithiated LCO electrode in Figure 5e, it is clearly found that the bright region with high conductivity (O3-II phase) moves inward on the (003) face region (O3-I phase). On the basis of the C-AFM measurement in Figure S5, we further confirmed that the bright boundary regions on the (003) face have a higher local work function comparing to the interior region. It is worth mentioning that the difference of current signal on different local regions are not due to the tip geometry or grain boundary effects.[59] The measured results in Figure 3, Figure 5c,e can be explained by the sketch of "shrinking core deintercalation models"[60,61] in Figure 5e,f. Although the Li-ions can move easily along the layer parallel to the (003) plane, it is hardly possible for them to penetrate through the close-packed O−Co−O layers. Thus, with the degree of delithiation increasing, the Li-ions inside the Li layers move outward along the Co−O inter-planes step by step, and the Li-ion deintercalation within the LCO grain proceeds from the outside in. Under a nonequilibrium deintercalation condition, the inside O3-I phase cannot be delithiated in time when the charging current is terminated at the achieved

DOI: 10.1021/acsami.9b11140
ACS Appl. Mater. Interfaces 2019, 11, 33043−33053

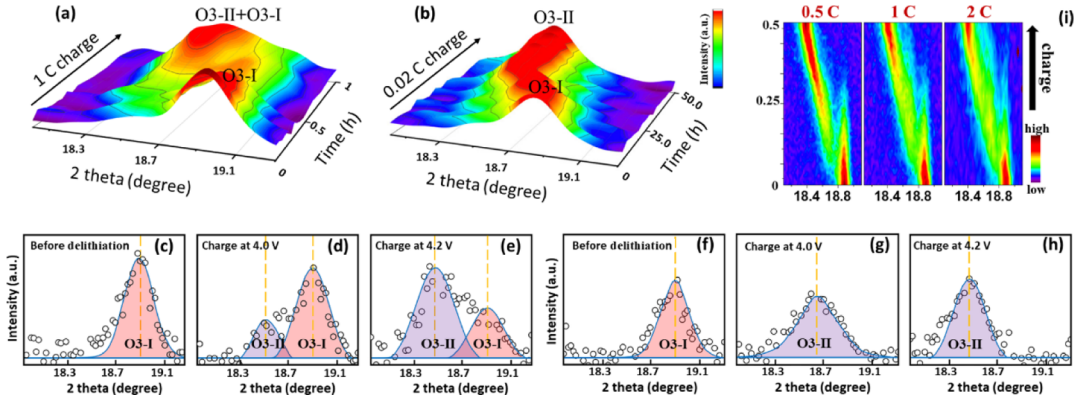

Figure 7. (a,b) 3D in situ XRD patterns of the (003) peaks of the LCO thin film during the first delithiation process at charging rates of 1 and 0.02 C, respectively. (c–e) Diffraction (003) peaks belonging to O3-I and O3-II phases before delithiation and with a charge voltage of V_c = 4.0, 4.2V for (a). (f–h) The diffraction (003) peaks belonging to O3-I and O3-II phases before delithiation and with a charge voltage of V_c = 4.0, 4.2V for (b). (i) In situ XRD of the (003) peaks of commercial LCO during the first deintercalation at different charging rates (x value is calculated from the same method reported in ref 47. x = 0 is the pristine sample, and x = 0.5 is considered as the fully charged sample).

charge potential before the diffusion process is completed. As a result, the edge region corresponding to the initial Li-ion deintercalation becomes a Li-poor region with high conductivity (O3-II phase). However, the inner local region corresponding to an underintercalated region (O3-I phase) or metastable lithium disordering intermediate phase[7] maintains the Li-rich state with low conductivity.

The ex situ C-AFM and time-dependent XRD characterization have confirmed that the intrinsic conductivity difference of insulated O3-I and metallic O3-II phases can be preserved in the post-mortem electrode. Ideally, the direct electron configuration measurement of LCO at different charge states can reveal the origin of the intrinsic conductivity change. As shown in Figure 6, by measuring the Co K-edge, L-edge, and O K-edge XAS spectra, the local environments and valence states of Co^+ and O^- can be studied.

Figure 6a displays the Co K-edge XAS spectra of $Li_{1-x}CoO_2$ with the degree of delithiation increases and the standard samples. The XAS spectra in Figure 6a include a pre-edge absorption peak (A), shoulder absorption peak (B), and a strong main absorption peak (C). The pre-edge absorption peak is attributed to the electric quadrupole-allowed and/or the electric dipole-forbidden transition of 1s electron to the 3d unoccupied orbital of the low-spin state ($t_{2g}^6e_g^0$) in the Co^{3+}. The intensity of the pre-edge depends on the degree of electric quadrupole and/or electric dipole (3d–4p orbital mixing). The gradual increase of the pre-edge peak intensities with the delithiated $Li_{1-x}CoO_2$ (see the inset in Figure 6a) indicates that noncentrosymmetric environment of the slightly distorted CoO_6 octahedral site from perfect octahedral geometry, especially for highly delithiated states (~4.2 V), suggests that lithium-ion deinsertion from the initial O3-I phase induces a small shift of the CoO_2 layer to follow the distortion of the oxygen lattice, and thus exists in a distorted octahedral environment.[62] The shoulder absorption peak can be assigned to dipole-allowed 1s → 4p transition with shakedown process by ligand-to-metal charge transfer without shakedown process and the main absorption edge features were attributed to purely dipole-allowed 1s → 4p transition without shakedown process.[63] The shoulder absorption peak disappears with the delithiated $Li_{1-x}CoO_2$, which suggests that lithium-ion deinsertion in $Li_{1-x}CoO_2$ hosts may induce local structural distortion. These observations support the probable availability of indirect information on the significant structural changes in the symmetry of the CoO_6 octahedral site in the O3-II phase. Further confirmation for this assignment comes from a comparison of the main absorption peak for $Li_{1-x}CoO_2$; the peak shift toward higher energy explains that Co ions can be oxidized to a high oxidation state with Li-ion deinsertion, which increases the electrostatic binding energy of core electrons. The oxidation of Co ions in the O3-II phase achieves an enhancement in charge transfer kinetics that leads to a lower charge-transfer resistance and further improved electrical conductivity in $Li_{1-x}CoO_2$.[64] Previous work by Michel et al. also supported that the metallic properties are finally induced because the holes in the Co ions' t_{2g} band will lead to a significant degree of screening.[11]

Figure 6b presents Co L3,2-edge XAS spectra of $Li_{1-x}CoO_2$ with the degree of delithiation increase. The Co L-edge causes the electron transitions from the Co 2p core hole to the 3d unoccupied states. The spin–orbit interaction of the Co 2p core hole splits the spectrum into two well-separated $2p_{3/2}$ (L3) and $2p_{1/2}$ (L2) spectral features. The peak position and the spectral line shape of the 3d metal L-edge strongly depend on the local atomic and electronic structures of the metal ions, and thus provide information about the electronic configuration and valence states. The inset in Figure 6b shows that the features at the Co L3,2-edge peaks are slightly shifted toward higher energy and give further asymmetric broadening with lithium-ion deinsertion. With the degree of delithiation increase, these observations give direct evidence that the Co ion participates in redistribution of charge (transfer and rehybridization between Co and O orbitals) in the charge compensation process.[63,65] Considering the condition for charge compensation, it can be suggested that the O3-I → O3-II phase transition leads to local structural rearrangement of the CoO_6 octahedral, which is consistent with the data of the Co K-edge XAS spectra. Furthermore, the magnitudes of the Co–O (about 1.5 Å) and Co–Co (about 2.4 Å) bonds change with different charge states, shown in Figure 6c. Here, these bond changes respond to the rehybridization of Co and O molecular orbitals. Figure 6d presents the O K-edge XAS spectra. The O K-edge XAS spectra of $Li_{1-x}CoO_2$ is characterized by three main feature peaks (A, B, and C). Peak A depends on the electron transition from the transition to hybridized states of O 2p orbitals with Co 3d orbitals, and

DOI: 10.1021/acsami.9b11140
ACS Appl. Mater. Interfaces 2019, 11, 33043–33053

the broad peaks B and C correspond to the transitions from the hybridization of the Co 4sp orbitals with the oxygen 2p orbital. With increasing degree of delithiation, the intensity of peak A increases gradually and two additional shoulder peaks A2 and A3 appear to broaden peak A. Therefore, the electronic configuration of the O atom in the interface of $Li_{1-x}CoO_2$ is changed. The broadening peak A manifests the enhancing O 2p−Co 3d hybridization under the Li ion removal from $Li_{1-x}CoO_2$, which results in a high probability for improving the transport of charge carriers.[66,67] To sum up, we supposed that the oxidation of Co ions and the increasing of O 2p−Co 3d hybridization in the O3-II phase achieve an enhancement in charge transfer kinetics, which leads to the electrical conductivity improvement in $Li_{1-x}CoO_2$.

The phase transformation hysteresis was commonly observed, and often interpreted as an inhomogeneous reaction within the electrode or micron monocrystal scale because of lack of characterization techniques with nanoscale resolution.[61,68] Recently, in situ transmission X-ray microscopy provided a method to observe the phase heterogeneity within a $LiCoO_2$ microparticle under the nonequilibrium de-/intercalation process.[44] It was confirmed that the nonequilibrium state of LCO reached by high-current-density delithiation differs from the equilibrium phases. Our ex situ time-dependence XRD and C-AFM studies on the thin-film electrode have shown that, after nonequilibrium deintercalation (about 1 C charging), the different local regions (Li-poor or -rich region) within an LCO nanograin can be observed. For further exploring the nonequilibrium phase transition in LCO thin-film cathodes, Figure 7a,b shows in situ (003) diffraction peaks of an LCO thin-film electrode during the first charge with charging rates of 1 and 0.02 C, respectively. Figure 7c−e shows the diffraction (003) peaks belonging to the O3-I and O3-II phases before delithiation and with a charge voltage of V_c = 4.0, 4.2 V for Figure 7a, respectively. From the figures, it is found that, in the charge process, the peak that belongs to the O3-II phase keeps growing and eventually becomes dominant. However, for both quick and slow charge cases with 1 and 0.02 C, the change of diffraction peaks with charge voltage appears evident difference. For 1 C, as seen in Figure 7a,e, there exists an overlapping doublet corresponding to the O3-I and O3-II phases at the end of charging. By contrast, for 0.02 C, as shown in Figure 7b,h, there is single peak belonging to O3-II at the end of charging. Therefore, the XRD results confirm that the LCO thin-film electrode with the (003) preferred orientation undergoes phase-transition hysteresis during the nonequilibrium deintercalation for the quick charge case. Similarly, Figure 7i shows in situ XRD patterns of the (003) peaks for commercial LCO electrode materials during the first deintercalation at 0.5, 1.0 and 2 C, respectively. From the figure, it is observed that, with the increase of charging rate, the O3-I/II coexisting region caused by the phase-transition hysteresis can also be expanded. Besides, the left shift of the O3-II diffraction peak with increasing charge voltage is observed in Figure 7c,b,e, which means that the lattice constant c of the O3-II phase is increased with the deintercalation of Li ions. This is because the removal of Li-ions in layered $Li_{1-x}CoO_2$ gives rise to the increase of the electrostatic repulsion force between the oxygen ions in adjacent layers.[18,19] Moreover, the increasing of the lattice constant c can inevitably result in the distortion of the CoO_6 octahedral or the change of the Co−O bond length, which is consistent with the above XAS measured results.

Figure 8a−d shows the sketch of the phase transformation model of the tLCO thin-film electrode with the (003)

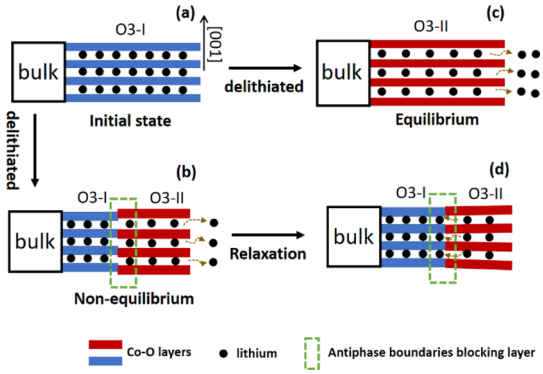

Figure 8. Sketches of a phase transformation model of the LCO thin-film electrode with the (003) preferred orientation. (a) Initial state, (b) nonequilibrium deintercalation, (c) equilibrium deintercalation, and (d) relaxation of nonequilibrium deintercalation.

preferred orientation forhe initial state, equilibrium deintercalation, nonequilibrium deintercalation, and its relaxation, respectively. As seen in Figure 8c, the LCO electrode charged under the close-equilibrium case undergoes a more uniform lattice expansion with a negligible antiphase boundary so that only the O3-II phase was found at the end of charge. However, nonequilibrium deintercalation will give rise to quite different results. The battery electrode charged at a high rate suffers from an additional overpotential. The higher the charging rate is, the higher the overpotential and charge voltage platforms are. Thus, a larger drive force is imposed in the lithium ions of the electrode materials.[47] Under nonequilibrium deintercalation, the colossal drive force will cause the sudden expansion of the Co−O layers, which results in the formation of antiphase boundaries,[27] as seen in Figure 8b. By the antiphase boundary, the LCO crystal is divided into both regions: Li-rich O3-I phase (left) and lattice-expanding Li-poor O3-II phase (right). Moreover, the antiphase boundary that is often created along the [001] direction will block the lithium diffusion channels.[69,70] At the same time, as found in Figure 8d, the relaxation of the overexpanded Co−O layers with the O3-II phase will cause the decrease of the lattice constant c and the backflow of lithium ions. Especially, the backflow of Li ions on the boundaries of the two phases would reduce the stress from lattice mismatch and the chemical potential difference between the O3-I and O3-II phases, which is in favor of the stability of the O3-I phase. Therefore, for a high charging rate, the nonequilibrium deintercalation will result in phase-transition hysteresis and the O3-I/II coexistence at the end of charging. These explain well the time- and charge rate-dependent XRD patterns in Figures 5a and 7. The similar phase separation under nonequilibrium deintercalation because of the ionic blockade layer has been found in $LiNi_{1/2}Mn_{3/2}O_4$.[40] At last, it is hoped that, based on this ionic blockade mechanism, the formation and movement of phase boundaries during the nonequilibrium de-/intercalation can be further studied by using in situ STEM and AFM.

4. CONCLUSIONS

The nonequilibrium phase transition and consequent IMT of the LCO thin-film electrode were studied. By using in situ PF-TUNA technique, the heterogeneous formation of a metallic

DOI: 10.1021/acsami.9b11140
ACS Appl. Mater. Interfaces 2019, 11, 33043−33053

O3-II phase on the insulated pristine LCO thin-film electrode was observed at the nanoscale during the deintercalation. It is also found that the metallic O3-II phase can sustain in the post-mortem LCO electrode, having a higher work function than the insulated O3-I phase. Moreover, based on XAS measurements, the metallic state of the O3-II phase is proved to result from the oxidation of Co ions and the increasing of the O 2p−Co 3d hybridization. At the same time, by in situ XRD characterization for different charge rates, it is found that nonequilibrium deintercalation with a high charge rate leads to phase-transition hysteresis and O3-I/II coexistence at the end of charging for LCO thin-film electrodes. An ionic blockade model with an antiphase boundary was suggested to explain this phase-transition hysteresis during high-rate charging. Our results present clearly the example for IMT characterization on solid/liquid interfaces at the nanoscale and open up the imaging of deintercalation-induced nonequilibrium phase transformations for layer-structured cathode for lithium-ion batteries. Lastly, we look forward to further studies, using in situ STEM and AFM, on the formation and movement of phase boundaries during nonequilibrium de-/intercalation, based on the ionic blockade mechanism.

■ ASSOCIATED CONTENT

Supporting Information

The Supporting Information is available free of charge on the ACS Publications website at DOI: 10.1021/acsami.9b11140.

Additional experimental and methodical details, as well as additional Raman, electrochemical performances, and C-AFM data (PDF)

■ AUTHOR INFORMATION

Corresponding Authors

*E-mail: ljx0721@qq.com (J.L.).
*E-mail: cldong@mail.tku.edu.tw (C.-L.D.).
*E-mail: zghuang@fjnu.edu.cn (Z.H.).

ORCID

Jiaxin Li: 0000-0001-5360-0219
Zhensheng Hong: 0000-0002-2567-4955
Chung-Li Dong: 0000-0002-4289-4677
Zhigao Huang: 0000-0002-8157-3550

Author Contributions

⊥Y.C. and Q.Y. contributed equally.

Notes

The authors declare no competing financial interest.

■ ACKNOWLEDGMENTS

The authors wish to acknowledge the financial support by the Natural Science Foundations of China (nos. 61574037, 11344008, 11204038) and the Natural Science Foundations of Fujian Province (no. 2017J01035).

■ REFERENCES

(1) Yan, P.; Zheng, J.; Zheng, J.; Wang, Z.; Teng, G.; Kuppan, S.; Xiao, J.; Chen, G.; Pan, F.; Zhang, J.-G.; Wang, C.-M. Ni and Co Segregations On Selective Surface Facets and Rational Design of Layered Lithium Transition-Metal Oxide Cathodes. *Adv. Energy Mater.* **2016**, *6*, 1502455.

(2) Kim, D.; Cho, M.; Cho, K. Rational Design of Na ($Li_{1/3}Mn_{2/3}$) O_2 Operated by Anionic Redox Reactions for Advanced Sodium-Ion Batteries. *Adv. Mater.* **2017**, *29*, 1701788.

(3) Yao, H.-R.; Wang, P.-F.; Gong, Y.; Zhang, J.; Yu, X.; Gu, L.; Ouyang, C.; Yin, Y.-X.; Hu, E.; Yang, X.-Q.; Stavitski, E.; Guo, Y.-G.; Wan, L.-J. Designing Air-Stable O3-Type Cathode Materials by Combined Structure Modulation for Na-Ion Batteries. *J. Am. Chem. Soc.* **2017**, *139*, 8440.

(4) He, P.; Yu, H.; Li, D.; Zhou, H. Layered Lithium Transition Metal Oxide Cathodes towards High Energy Lithium-Ion Batteries. *J. Mater. Chem.* **2012**, *22*, 3680−3695.

(5) Mizushima, K.; Jones, P. C.; Wiseman, P. J.; Goodenough, J. B. Li_xCoC_2 (0<X<-1): A New Cathode Material for Batteries of High Energy Density. *Mater. Res. Bull.* **1980**, *15*, 783−789.

(6) Terasaki, I.; Sasago, Y.; Uchinokura, K. Large Thermoelectric Power in $NaCo_2O_4$ Single Crystals. *Phys. Rev. B: Condens. Matter Mater. Phys.* **1997**, *56*, R12685.

(7) Miyoshi, K.; Manami, K.; Sasai, R.; Nishigori, S.; Takeuchi, J. Electronic States Realized by the Interplay Between Li Diffusion and Co^{3+}/Co^{4+} Charge Ordering in Li_xCoO_2. *Phys. Rev. B: Condens. Matter Mater. Phys.* **2018**, *98*, 195106.

(8) Motohashi, T.; Sugimoto, Y.; Masubuchi, Y.; Sasagawa, T.; Koshibae, W.; Tohyama, T.; Yamauchi, H.; Kikkawa, S. Impact of Lithium Composition on the Thermoelectric Properties of the Layered Cobalt Oxide System Li_xCoO_2. *Phys. Rev. B: Condens. Matter Mater. Phys.* **2011**, *83*, 195128.

(9) Miyoshi, K.; Iwai, C.; Kondo, H.; Miura, M.; Nishigori, S.; Takeuchi, J. Magnetic and Electronic Properties of Li_xCoO_2 Single Crystals. *Phys. Rev. B: Condens. Matter Mater. Phys.* **2010**, *82*, 075113.

(10) Kang, H.; Lee, J.; Rodgers, T.; Shim, J.-H.; Lee, S. Electrical Conductivity of Delithiated Lithium Cobalt Oxides: Conductive Atomic Force Microscopy and Density Functional Theory Study. *J. Phys. Chem. C* **2019**, *123*, 17703−17710.

(11) Ménétrier, M.; Saadoune, I.; Levasseur, S.; Delmas, C. The Insulator-Metal Transition upon Lithium Deintercalation from $LiCoO_2$: Electronic Properties and 7Li Nmr Study. *J. Mater. Chem.* **1999**, *9*, 1135−1140.

(12) Marianetti, C. A.; Kotliar, G.; Ceder, G. A First-Order Mott Transition in Li_xCoO_2. *Nat. Mater.* **2004**, *3*, 627−631.

(13) Milewska, A.; Świerczek, K.; Tobola, J.; Boudoire, F.; Hu, Y.; Bora, D. K.; Mun, B. S.; Braun, A.; Molenda, J. The Nature of the Nonmetal−Metal Transition in Li_xCoO_2 Oxide. *Solid State Ionics* **2014**, *263*, 110−118.

(14) Van der Ven, A.; Aydinol, M. K.; Ceder, G.; Kresse, G.; Hafner, J. First-Principles Investigation of Phase Stability in Li_xCoO_2. *Phys. Rev. B: Condens. Matter Mater. Phys.* **1998**, *58*, 2975−2987.

(15) Xia, H.; Lu, L.; Meng, Y. S.; Ceder, G. Phase Transitions and High-Voltage Electrochemical Behavior of $LiCoO_2$ Thin Films Grown by Pulsed Laser Deposition. *J. Electrochem. Soc.* **2007**, *154*, A337.

(16) Yang, X. Q.; Sun, X.; McBreen, J. New Phases and Phase Transitions Observed in $Li_{1-X}CoO_2$ during Charge: In Situ Synchrotron X-Ray Diffraction Studies. *Electrochem. Commun.* **2000**, *2*, 100−103.

(17) Lu, X.; Sun, Y.; Jian, Z.; He, X.; Gu, L.; Hu, Y.-S.; Li, H.; Wang, Z.; Chen, W.; Duan, X.; Chen, L.; Maier, J.; Tsukimoto, S.; Ikuhara, Y. New Insight Into the Atomic Structure of Electrochemically Delithiated O3 $Li_{(1-X)}CoO_2(0\leq x\leq 0.5)$ Nanoparticles. *Nano Lett.* **2012**, *12*, 6192−6197.

(18) Ueda, A.; Ohzuku, T. Solid-State Redox Reactions of $LiNi_{1/2}Co_{1/2}O_2$ ($R\bar{3}M$) for 4 Volt Secondary Lithium Cells. *J. Electrochem. Soc.* **1994**, *141*, 2010−2014.

(19) Reimers, J. N.; Dahn, J. R. Electrochemical and in Situ X-Ray Diffraction Studies of Lithium Intercalation in Li_XCoO_2. *J. Electrochem. Soc.* **1992**, *139*, 2091−2097.

(20) Sharma, N.; Peterson, V. K.; Elcombe, M. M.; Avdeev, M.; Studer, A. J.; Blagojevic, N.; Yusoff, R.; Kamarulzaman, N. Structural Changes in a Commercial Lithium-Ion Battery During Electrochemical Cycling: An in Situ Neutron Diffraction Study. *J. Power Sources* **2010**, *195*, 8258−8266.

(21) Shimoda, K.; Murakami, M.; Takamatsu, D.; Arai, H.; Uchimoto, Y.; Ogumi, Z. In Situ NMR Observation of the Lithium

DOI: 10.1021/acsami.9b11140
ACS Appl. Mater. Interfaces 2019, 11, 33043−33053

Extraction/Insertion from $LiCoO_2$ Cathode. *Electrochim. Acta* **2013**, *108*, 343−349.
(22) Jiang, D.; Jiang, Y.; Li, Z.; Liu, T.; Wo, X.; Fang, Y.; Tao, N.; Wang, W.; Chen, H.-Y. Optical Imaging of Phase Transition and Li-Ion Diffusion Kinetics of Single $LiCoO_2$ Nanoparticles During Electrochemical Cycling. *J. Am. Chem. Soc.* **2017**, *139*, 186−192.
(23) Ben Yahia, H.; Shikano, M.; Kobayashi, H. Phase Transition Mechanisms in Li_xCoO_2 ($0.25 \leq X \leq 1$) Based On Group-Subgroup Transformations. *Chem. Mater.* **2013**, *25*, 3687−3701.
(24) Yang, S.-H.; Weill, F.; Croguennec, L.; Carlier, D.; Ménétrier, M.; Delmas, C. Lithium and Vacancy Ordering in Li_xCoO_2 Derived From O2-Type $LiCoO_2$. *Chem. Mater.* **2003**, *15*, 2977−2983.
(25) Carlier, D.; Van der Ven, A.; Delmas, C.; Ceder, G. First-Principles Investigation of Phase Stability in the O2-$LiCoO_2$ System. *Chem. Mater.* **2003**, *15*, 2651−2660.
(26) Huang, J. Y.; Zhong, L.; Wang, C. M.; Sullivan, J. P.; Xu, W.; Zhang, L. Q.; Mao, S. X.; Hudak, N. S.; Liu, X. H.; Subramanian, A.; Fan, H.; Qi, L.; Kushima, A.; Li, J. In Situ Observation of the Electrochemical Lithiation of a Single SnO_2 Nanowire Electrode. *Science* **2010**, *330*, 1515−1520.
(27) Gong, Y.; Zhang, J.; Jiang, L.; Shi, J.-A.; Zhang, Q.; Yang, Z.; Zou, D.; Wang, J.; Yu, X.; Xiao, R.; Hu, Y.-S.; Gu, L.; Li, H.; Chen, L. In Situ Atomic-Scale Observation of Electrochemical Delithiation Induced Structure Evolution of $LiCoO_2$ Cathode in a Working All-Solid-State Battery. *J. Am. Chem. Soc.* **2017**, *139*, 4274−4277.
(28) Liu, T.; Lin, L.; Bi, X.; Tian, L.; Yang, K.; Liu, J.; Li, M.; Chen, Z.; Lu, J.; Amine, K.; Xu, K.; Pan, F. In Situ Quantification of Interphasial Chemistry in Li-Ion Battery. *Nat. Nanotechnol.* **2019**, *14*, 50−56.
(29) Balke, N.; Jesse, S.; Morozovska, A. N.; Eliseev, E.; Chung, D. W.; Kim, Y.; Adamczyk, L.; García, R. E.; Dudney, N.; Kalinin, S. V. Nanoscale Mapping of Ion Diffusion in a Lithium-Ion Battery Cathode. *Nat. Nanotechnol.* **2010**, *5*, 749−754.
(30) Wang, S.; Liu, Q.; Zhao, C.; Lv, F.; Qin, X.; Du, H.; Kang, F.; Li, B. Advances in Understanding Materials for Rechargeable Lithium Batteries by Atomic Force Microscopy. *Energy Environ. Mater.* **2018**, *1*, 28−40.
(31) Ramdon, S.; Bhushan, B.; Nagpure, S. C. In Situ Electrochemical Studies of Lithium-Ion Battery Cathodes Using Atomic Force Microscopy. *J. Power Sources* **2014**, *249*, 373−384.
(32) Yan, R.; Ghilane, J.; Phuah, K. C.; Pham Truong, T. N.; Adams, S.; Randriamahazaka, H.; Wang, Q. Determining Li^+-Coupled Redox Targeting Reaction Kinetics of Battery Materials with Scanning Electrochemical Microscopy. *J. Phys. Chem. Lett.* **2018**, *9*, 491−496.
(33) Sun, T.; Wang, D.; Mirkin, M. V. Tunneling Mode of Scanning Electrochemical Microscopy: Probing Electrochemical Processes at Single Nanoparticles. *Angew. Chem., Int. Ed.* **2018**, *57*, 7463−7467.
(34) Nellist, M. R.; Laskowski, F. A. L.; Qiu, J.; Hajibabaei, H.; Sivula, K.; Hamann, T. W.; Boettcher, S. W. Potential-Sensing Electrochemical Atomic Force Microscopy for in Operando Analysis of Water-Splitting Catalysts and Interfaces. *Nat. Energy* **2018**, *3*, 46−52.
(35) Stetson, C.; Yoon, T.; Coyle, J.; Nemeth, W.; Young, M.; Norman, A.; Pylypenko, S.; Ban, C.; Jiang, C.-S.; Al-Jassim, M.; Burrell, A. Three-Dimensional Electronic Resistivity Mapping of Solid Electrolyte Interphase On Si Anode Materials. *Nano Energy* **2019**, *55*, 477−485.
(36) Nellist, M. R.; Chen, Y.; Mark, A.; Gödrich, S.; Stelling, C.; Jiang, J.; Poddar, R.; Li, C.; Kumar, R.; Papastavrou, G.; Retsch, M.; Brunschwig, B. S.; Huang, Z.; Xiang, C.; Boettcher, S. W. Atomic Force Microscopy with Nanoelectrode Tips for High Resolution Electrochemical, Nanoadhesion and Nanoelectrical Imaging. *Nanotechnology* **2017**, *28*, 095711.
(37) Verde, M. G.; Baggetto, L.; Balke, N.; Veith, G. M.; Seo, J. K.; Wang, Z.; Meng, Y. S. Elucidating the Phase Transformation of $Li_4Ti_5O_{12}$ Lithiation at the Nanoscale. *ACS Nano* **2016**, *10*, 4312−4321.
(38) Etacheri, V.; Marom, R.; Elazari, R.; Salitra, G.; Aurbach, D. Challenges in the Development of Advanced Li-Ion Batteries: A Review. *Energy Environ. Sci.* **2011**, *4*, 3243−3262.
(39) Kang, K.; Meng, Y. S.; Bréger, J.; Grey, C. P.; Ceder, G. Electrodes with High Power and High Capacity for Rechargeable Lithium Batteries. *Science* **2006**, *311*, 977−980.
(40) Singer, A.; Ulvestad, A.; Cho, H.-M.; Kim, J. W.; Maser, J.; Harder, R.; Meng, Y. S.; Shpyrko, O. G. Nonequilibrium Structural Dynamics of Nanoparticles in $LiNi_{1/2}Mn_{3/2}O_4$ Cathode Under Operando Conditions. *Nano Lett.* **2014**, *14*, 5295−5300.
(41) Zhang, X.; Verhallen, T. W.; Labohm, F.; Wagemaker, M. Direct Observation of Li-Ion Transport in Electrodes Under Nonequilibrium Conditions Using Neutron Depth Profiling. *Adv. Energy Mater.* **2015**, *5*, 1500498.
(42) Ulvestad, A.; Singer, A.; Clark, J. N.; Cho, H. M.; Kim, J. W.; Harder, R.; Maser, J.; Meng, Y. S.; Shpyrko, O. G. Topological Defect Dynamics in Operando Battery Nanoparticles. *Science* **2015**, *348*, 1344−1347.
(43) Zhang, W.; Yu, H.-C.; Wu, L.; Liu, H.; Abdellahi, A.; Qiu, B.; Bai, J.; Orvananos, B.; Strobridge, F. C.; Zhou, X.; Liu, Z.; Ceder, G.; Zhu, Y.; Thornton, K.; Grey, C. P.; Wang, F. Localized Concentration Reversal of Lithium During Intercalation Into Nanoparticles. *Sci. Adv.* **2018**, *4*, No. eaao2608.
(44) Xu, Y.; Hu, E.; Zhang, K.; Wang, X.; Borzenets, V.; Sun, Z.; Pianetta, P.; Yu, X.; Liu, Y.; Yang, X.-Q.; Li, H. In Situ Visualization of State-of-Charge Heterogeneity within a $LiCoO_2$ Particle that Evolves upon Cycling at Different Rates. *ACS Energy Lett.* **2017**, *2*, 1240−1245.
(45) Sharma, N.; Guo, X.; Du, G.; Guo, Z.; Wang, J.; Wang, Z.; Peterson, V. K. Direct Evidence of Concurrent Solid-Solution and Two-Phase Reactions and the Nonequilibrium Structural Evolution of $LiFePO_4$. *J. Am. Chem. Soc.* **2012**, *134*, 7867−7873.
(46) Malik, R.; Zhou, F.; Ceder, G. Kinetics of Non-Equilibrium Lithium Incorporation in $LiFePO_4$. *Nat. Mater.* **2011**, *10*, 587.
(47) Zhou, Y.-N.; Yue, J.-L.; Hu, E.; Li, H.; Gu, L.; Nam, K.-W.; Bak, S.-M.; Yu, X.; Liu, J.; Bai, J.; Dooryhee, E.; Fu, Z.-W.; Yang, X.-Q. High-Rate Charging Induced Intermediate Phases and Structural Changes of Layer-Structured Cathode for Lithium-Ion Batteries. *Adv. Energy Mater.* **2016**, *6*, 1600597.
(48) Zhou, F. First-principles prediction of redox potentials in transition-metal compounds with LDA+U. *Phys. Rev. B: Condens. Matter Mater. Phys.* **2004**, *70*, 235121.
(49) Tintignac, S.; Baddour-Hadjean, R.; Pereira-Ramos, J.-P.; Salot, R. High Performance Sputtered $LiCoO_2$ Thin Films Obtained at a Moderate Annealing Treatment Combined to a Bias Effect. *Electrochim. Acta* **2012**, *60*, 121−129.
(50) Tintignac, S.; Baddour-Hadjean, R.; Pereira-Ramos, J. P.; Salot, R. Electrochemical Properties of High Rate Bias Sputtered $LiCoO_2$ Thin Films in Liquid Electrolyte. *J. Power Sources* **2014**, *245*, 76−82.
(51) Jeon, S.-W.; Lim, J.-K.; Lim, S.-H.; Lee, S.-M. As-Deposited $LiCoO_2$ Thin Film Cathodes Prepared by RF Magnetron Sputtering. *Electrochim. Acta* **2005**, *51*, 268−273.
(52) Liao, C.-L.; Fung, K.-Z. Lithium Cobalt Oxide Cathode Film Prepared by RF Sputtering. *J. Power Sources* **2004**, *128*, 263−269.
(53) Lu, W.; Zhang, J.; Xu, J.; Wu, X.; Chen, L. In Situ Visualized Cathode Electrolyte Interphase On $LiCoO_2$ in High Voltage Cycling. *ACS Appl. Mater. Interfaces* **2017**, *9*, 19313−19318.
(54) van Elp, J.; Wieland, J. L.; Eskes, H.; Kuiper, P.; Sawatzky, G. A.; FM, D. G.; Turner, T. S. Electronic Structure of CoO, Li-Doped CoO, and $LiCoO_2$. *Phys. Rev. B: Condens. Matter Mater. Phys.* **1991**, *44*, 6090.
(55) Ensling, D.; Thissen, A.; Laubach, S.; Schmidt, P. C.; Jaegermann, W. Electronic Structure of $LiCoO_2$ Thin Films: A Combined Photoemission Spectroscopy and Density Functional Theory Study. *Phys. Rev. B: Condens. Matter Mater. Phys.* **2010**, *82*, 195431.
(56) Ensling, D.; Cherkashinin, G.; Schmid, S.; Bhuvaneswari, S.; Thissen, A.; Jaegermann, W. Nonrigid Band Behavior of the

DOI: 10.1021/acsami.9b11140
ACS Appl. Mater. Interfaces 2019, 11, 33043−33053

Electronic Structure of $LiCoO_2$ Thin Film During Electrochemical Li Deintercalation. *Chem. Mater.* **2014**, *26*, 3948−3956.
(57) Rosolen, J. M.; Decker, F. Photoelectrochemical Behavior of $LiCoO_2$ Membrane Electrode. *J. Electroanal. Chem.* **2001**, *501*, 253−259.
(58) Tanida, H.; Yamashige, H.; Orikasa, Y.; Gogyo, Y.; Arai, H.; Uchimoto, Y.; Ogumi, Z. Elucidating the Driving Force of Relaxation of Reaction Distribution in $LiCoO_2$ and $LiFePO_4$ Electrodes Using X-Ray Absorption Spectroscopy. *J. Phys. Chem. C* **2016**, *120*, 4739−4743.
(59) Zhu, X.; Ong, C. S.; Xu, X.; Hu, B.; Shang, J.; Yang, H.; Katlakunta, S.; Liu, Y.; Chen, X.; Pan, L.; Ding, J.; Li, R. Direct Observation of Lithium-Ion Transport Under an Electrical Field in $LiCoO_2$ Nanograins. *Sci. Rep.* **2013**, *3*, 1084.
(60) Wilson, J. R.; Cronin, J. S.; Barnett, S. A.; Harris, S. J. Measurement of Three-Dimensional Microstructure in a $LiCoO_2$ Positive Electrode. *J. Power Sources* **2011**, *196*, 3443−3447.
(61) Ou-Yang, T. Y.; Huang, F.; Shu, G. J.; Lee, W. L.; Chu, M.; Liu, H. L.; Chou, F. C. Electronic Phase Diagram of Li_XCoO_2 Revisited with Potentiostatically Deintercalated Single Crystals. *Phys. Rev. B: Condens. Matter Mater. Phys.* **2012**, *85*, 35120.
(62) Didier, C.; Guignard, M.; Suchomel, M. R.; Carlier, D.; Darriet, J.; Delmas, C. Thermally and Electrochemically Driven Topotactical Transformations in Sodium Layered Oxides Na_xVO_2. *Chem. Mater.* **2016**, *28*, 1462−1471.
(63) Chen, C.-H.; Hwang, B.-J.; Chen, C.-Y.; Hu, S.-K.; Chen, J.-M.; Sheu, H.-S.; Lee, J.-F. Soft X-Ray Absorption Spectroscopy Studies On the Chemically Delithiated Commercial $LiCoO_2$ Cathode Material. *J. Power Sources* **2007**, *174*, 938−943.
(64) Cao, K.; Jiao, L.; Liu, Y.; Liu, H.; Wang, Y.; Yuan, H. Ultra-High Capacity Lithium-Ion Batteries with Hierarchical CoO Nanowire Clusters as Binder Free Electrodes. *Adv. Funct. Mater.* **2015**, *25*, 1082−1089.
(65) Wolverton, C.; Zunger, A. First-Principles Prediction of Vacancy Order-Disorder and Intercalation Battery Voltages in Li_xCoO_2. *Phys. Rev. Lett.* **1998**, *81*, 606−609.
(66) Zhu, M. W.; Wang, H. L.; Lei, H.; Zhang, Y. J.; Jia, N.; Wang, Z. J. Strain-Induced Modification in Microstructure and Electrical Properties of Polycrystalline $LaNiO_3$-Delta Films. *Appl. Phys. A: Mater. Sci. Process.* **2016**, *122*, 364.
(67) Tsubouchi, K.; Ohkubo, I.; Kumigashira, H.; Matsumoto, Y.; Ohnishi, T.; Lippmaa, M.; Koinuma, H.; Oshima, M. Epitaxial Growth and Surface Metallic Nature of $LaNiO_3$ Thin Films. *Appl. Phys. Lett.* **2008**, *92*, 262109.
(68) Nakamura, T.; Watanabe, T.; Kimura, Y.; Amezawa, K.; Nitta, K.; Tanida, H.; Ohara, K.; Uchimoto, Y.; Ogumi, Z. Visualization of Inhomogeneous Reaction Distribution in the Model $LiCoO_2$ Composite Electrode of Lithium Ion Batteries. *J. Phys. Chem. C* **2017**, *121*, 2118−2124.
(69) Yang, Z.; Ong, P.; He, Y.; Wang, L.; Bowden, M. E.; Xu, W.; Droubay, T. C.; Wang, C.; Sushko, P. V.; Du, Y. Direct Visualization of Li Dendrite Effect On $LiCoO_2$ Cathode by in Situ Tem. *Small* **2018**, *14*, 1803108.
(70) Moriwake, H.; Kuwabara, A.; Fisher, C. A. J.; Huang, R.; Hitosugi, T.; Ikuhara, Y. H.; Oki, H.; Ikuhara, Y. First-Principles Calculations of Lithium-Ion Migration at a Coherent Grain Boundary in a Cathode Material, $LiCoO_2$. *Adv. Mater.* **2013**, *25*, 618−622.

DOI: 10.1021/acsami.9b11140
ACS Appl. Mater. Interfaces 2019, 11, 33043−33053